


PAPER • OPEN ACCESS

## Effects of laser scanning strategies on selective laser melting of pure tungsten

To cite this article: Dongdong Gu *et al* 2020 *Int. J. Extrem. Manuf.* **2** 025001

View the [article online](#) for updates and enhancements.

# Effects of laser scanning strategies on selective laser melting of pure tungsten

Dongdong Gu<sup>1,2</sup> , Meng Guo<sup>1,2</sup>, Hongmei Zhang<sup>1,2</sup>, Yixuan Sun<sup>1,2</sup>, Rui Wang<sup>1,2</sup> and Lei Zhang<sup>1,2</sup>

<sup>1</sup> College of Materials Science and Technology, Nanjing University of Aeronautics and Astronautics, Yudao Street 29, Nanjing 210016, Jiangsu Province, People's Republic of China

<sup>2</sup> Jiangsu Provincial Engineering Laboratory for Laser Additive Manufacturing of High-Performance Metallic Components, Nanjing University of Aeronautics and Astronautics, Yudao Street 29, Nanjing 210016, Jiangsu Province, People's Republic of China

E-mail: [dongdonggu@nuaa.edu.cn](mailto:dongdonggu@nuaa.edu.cn)

Received 19 December 2019, revised 7 February 2020

Accepted for publication 28 February 2020

Published 23 March 2020



## Abstract

Three types of scanning strategies, including the chessboard scanning strategy, the zigzag scanning strategy and the remelting scanning strategy, were conducted to study the effects of scanning strategies on surface morphology, microstructure, mechanical properties and the grain orientation of selective laser melted pure tungsten. The results showed that the pores and cracks were main defects in SLM-processed tungsten parts. The pores could be eliminated using the remelting scanning strategy. However, the cracks seemed to be inevitable regardless of the applied scanning strategies. The microstructures of SLM-processed tungsten were columnar grains and showed strong epitaxial growth along the building direction. A compressive strength of 923 MPa with an elongation of 7.7% was obtained when the zigzag scanning strategy was applied, which was the highest among the three scanning strategies. By changing the scanning strategies, the texture of SLM-processed tungsten in the direction of processing could be changed.

**Keywords:** scanning strategy, selective laser melting, pure tungsten, microstructure, compressive strength, texture

(Some figures may appear in colour only in the online journal)

## 1. Introduction

With the development of the industry technology, the problem of energy is getting more and more attention. Nowadays, the nuclear fusion energy becomes more and more popular for its green, low carbon and sustainable development [1, 2]. However, the critical challenge that hinders the development of nuclear fusion energy is the plasma facing materials (PFMs) [3]. The harsh service environment such as high temperature and radiation environment brings higher requirement for materials. As the metal with the highest

melting point on earth, tungsten (W) is outstanding due to its high melting point, excellent heat conductivity, high sputtering threshold and low tritium retention [4]. Consequently, tungsten is regarded as a promising candidate material for PFMs that can withstand the extreme service environments [5, 6]. However, as a typical brittle material, tungsten has nearly no ductility at room temperature, which limits its applications as structural material [7, 8]. Due to its high hardness and big brittleness, tungsten is very difficult to be machined into components. Traditionally, tungsten is produced by powder metallurgy, spark plasma sintering and powder injection molding [9–11]. However, these methods share a common shortcoming that they fail to fabricate complex parts due to the limitation of processing conditions.

Since the appearance of additive manufacturing technology (AM), tremendous changes have taken place in



Original content from this work may be used under the terms of the [Creative Commons Attribution 3.0 licence](https://creativecommons.org/licenses/by/3.0/). Any further distribution of this work must maintain attribution to the author(s) and the title of the work, journal citation and DOI.

manufacturing. Now, special structures at the micro and nanoscale can be manufactured [12]. As a relatively new AM technology, selective laser melting was successfully used to manufacture metals parts. Up to now, metal materials such as aluminum alloys, titanium alloys, nickel base superalloys and stainless steels have been maturely fabricated by SLM [13–21]. Some structural components with complex geometrical shapes manufactured by SLM have been widely applied in aerospace engineering and bioengineering. These cases demonstrate that selective laser melting is a promising AM technology. During SLM, a laser beam with high energy selectively melts the metal powder in a protective gas atmosphere. The laser beam moves according to the 2D patterns sliced on a 3D model. In the SLM process, the molten metal rapidly solidifies and forms continuous molten pools. As the molten pools move, a single layer is shaped. Through overlapping layer by layer, the 3D component is ultimately formed. As calculated by Wang *et al* [22], a highest temperature of 7300 K could be obtained by adjusting the processing parameters. In this situation, even the refractory metals such as tungsten (W), tantalum (Ta) and molybdenum (Mo) can be completely melt by a high-energy laser beam [23–27]. However, the SLM process involves a series of complex physical and chemical phenomena such as the absorption and reflection of laser energy, heat conduction, phase transition and melt flow. These complex phenomena occur along with the rapid melting and solidification processes. For tungsten, high melting point (3420 °C) will need high energy input to achieve complete melting. High surface tension and high viscosity can facilitate the balling phenomenon. Moreover, high ductile-to-brittle transition temperature (DBTT) can result in the formation of cracks during rapid cooling in the SLM process. Therefore, selective laser melting of pure tungsten has always been a challenge. Previous research on SLM-processed pure tungsten demonstrated that the densification behavior could be regulated by matching the processing parameters reasonably [28, 29]. However, the cracks seemed to be inevitable in SLM-processed pure tungsten. The previous works mainly focus on the effect of processing parameters such as laser power, scanning speed, layer thickness and hatch spacing. However, the effects of scanning strategy are still unknown. As a vital processing parameter in SLM, scanning strategy has a significant impact on the formation of grain structure and crystallographic texture. The essential characteristics of overlapping layer-by-layer and high thermal gradient in the SLM process are easy to result in preferential growth of crystals, while the laser scanning strategy can significantly influence the heat transfer and lead to different microstructural evolution. Thus, selecting an appropriate scanning strategy can facilitate the formation of homogeneous microstructure and enhance mechanical properties. Recently, extensive studies have been conducted to understand the effects of different scanning strategies. Among these alloys, nickel-based alloys, 316L stainless steel and aluminum alloys are the most studied [30–33]. Geiger *et al* demonstrated that using a specific scanning strategy could tailor the texture of SLM-processed IN738LC alloy and obtained microstructures with elastic

anisotropy [34]. Yazza *et al* reported that laser remelting could improve the surface quality and enhance the densification level of SLM-processed 316L stainless steel parts [35]. The laser remelting scanning strategy has the ability of eliminating the surface contaminants and form good metallurgical bonding. Dai *et al* also verified that the laser remelting was an efficient method to eliminate the residual pores and promote the formation of high densification in SLM-processed AlSi12 [36]. For SLM-processed tungsten, the researches on scanning strategies were rarely reported. Zhou *et al* studied the effect of multiple laser scanning including no remelting, one additional scan for remelting and two additional scans for remelting [37]. He found that the balling phenomenon was weakened and the solidified surface became smoother using the remelting scanning strategy. Wang *et al* utilized three types of scanning strategies including no rotation without remelting, rotation without remelting and rotation with remelting [22]. He pointed out that the pattern of longitudinal cracks could be changed by scanning rotation. However, the cracks were unable to be suppressed regardless of the scanning strategy. In view of the previous works, no unified scanning strategy has been adopted that can be applicable for tungsten due to the character of the material itself.

In this work, pure tungsten was fabricated by SLM using three types of scanning strategies. The laser scanning strategies were chessboard scanning strategy (the so-called island scanning strategy), zigzag scanning strategy and remelting scanning strategy, respectively. The effects of scanning strategies on the surface morphology, microstructure and compressive properties were investigated in detail. The crystallographic texture and formation mechanism of grain structures along the build direction were discussed. This work provides a guidance for the selection of scanning strategy for selective laser melting of tungsten parts.

## 2. Materials and methods

### 2.1. Material preparation

Bulk tungsten parts were fabricated by SLM using the commercial and spherical tungsten powder. The range of the powder particles is from 5 to 25  $\mu\text{m}$  (figure 1(a)). The SLM equipment is consisted of a YLR-500 with a spot size of 70  $\mu\text{m}$ , an automatic powder spreading device, a process control system and an inert argon gas protection system. The schematic diagram of SLM process is shown in figure 1(b). The chessboard scanning strategy, zigzag scanning strategy and remelting scanning strategy were applied to fabricate pure tungsten, respectively (figure 2). The island in chessboard scanning strategy had a dimension of 5 mm  $\times$  5 mm. To reduce the residual stress, rotating 67° was applied between each layer. Rotating layer by layer could minimize the stacking overlap and rotating the thermal gradient as diverse as possible, further reducing the residual stress. Rotation of 67° was also applied by Wang *et al* [38] and Braun *et al* [39]. The laser power, scanning speed, layer thickness and

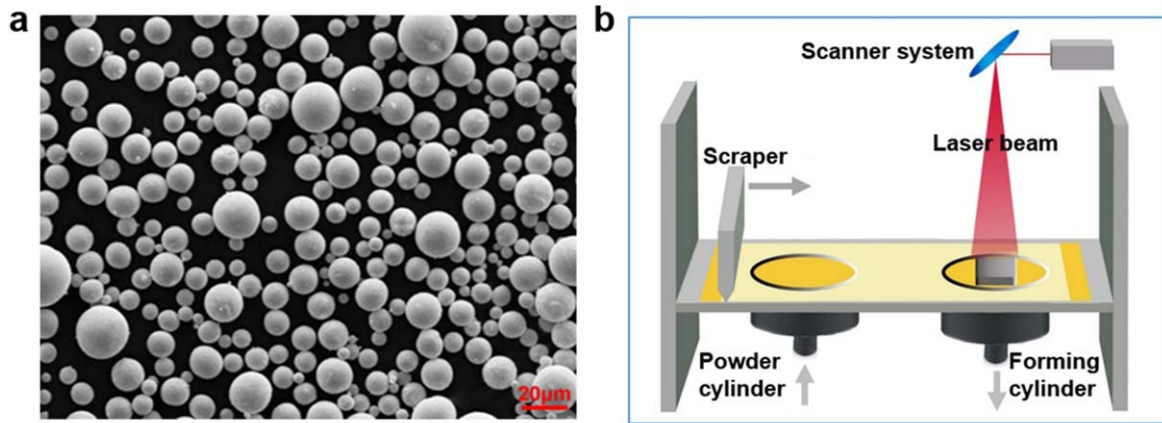


**Figure 1.** (a) SEM image of pure tungsten powder in this work, (b) schematic diagram of the SLM process.

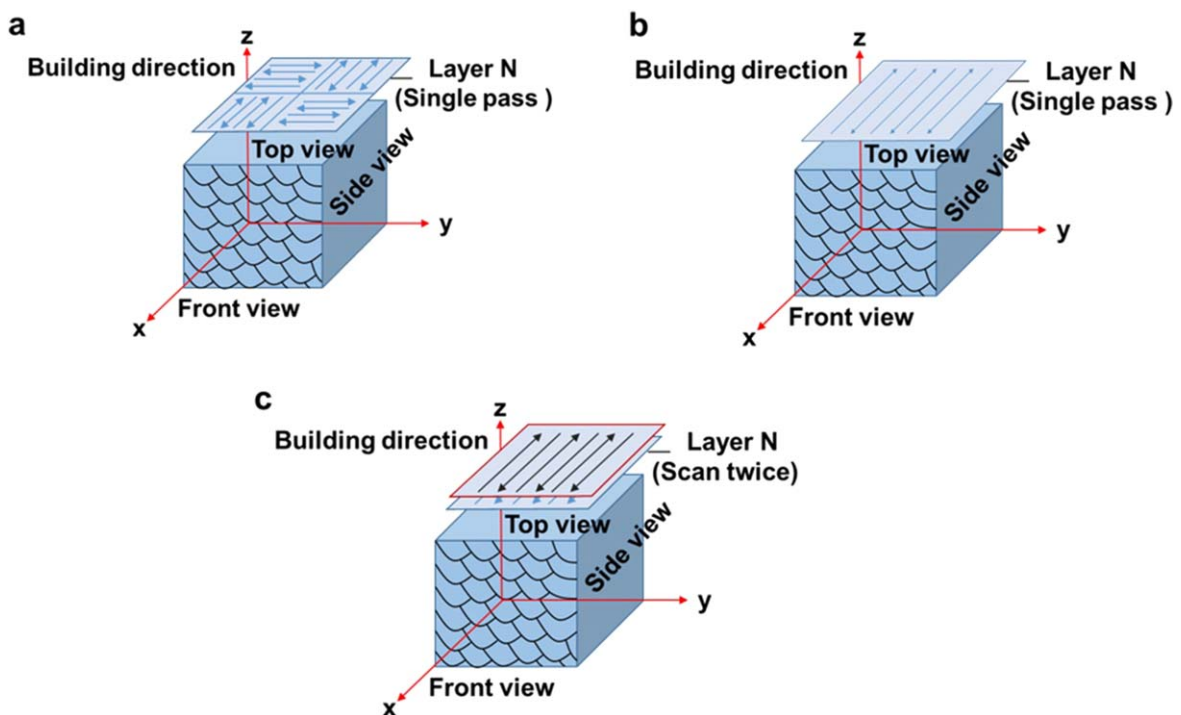


**Figure 2.** The applied scanning strategies in this work: (a) chessboard scanning strategy, (b) zigzag scanning strategy, (c) remelting scanning strategy.

hatch spacing were 300 W,  $300 \text{ mm s}^{-1}$ ,  $20 \text{ μm}$  and  $50 \text{ μm}$ , respectively, which was optimized in our previous works [40]. The processing parameters were the same for three types of scanning strategies. The dimensions of the cuboid samples were  $10 \text{ mm} \times 10 \text{ mm} \times 5 \text{ mm}$ . The cylindrical compressive testing parts having a diameter of 8 mm, a length of 10 mm, and a length to diameter of 1.25, as proposed by GB/T 7314-2017, were constructed.

## 2.2. Material characterization and mechanical tests

After the SLM process, the specimens were cut parallel to the steel substrate. The samples were ground and polished according to the standard metallographic testing procedures. The microstructures of front views and top views of individual parts were characterized using a MDS400 optical

microscopy (Chongqing Optec Instrument Co., Ltd, China). For the better observations of microstructure, the polished surface was etched by a solution composing HF (10 ml),  $\text{HNO}_3$  (30 ml) and distilled water (70 ml) for 25 s. The morphologies of top view and fracture surface morphologies were detected by a FEI Quanta 200 scanning electron microscope (SEM). For the analysis of the crystallographic texture, an electron backscatter diffraction (EBSD) mounted on a NANO SEM 430 (FEI, Hillsboro, Oregon) was employed. The step size taken for the EBSD analysis was  $1.1 \text{ μm}$ . In the band contrast (BC) maps, a misorientation of grain boundaries exceeding  $15^\circ$  was in black and grain boundaries with misorientation less than  $15^\circ$  were in red. An HXS-1000AY microhardness tester (AMETEK, Shanghai, China) was employed to measure the Vickers hardness. The



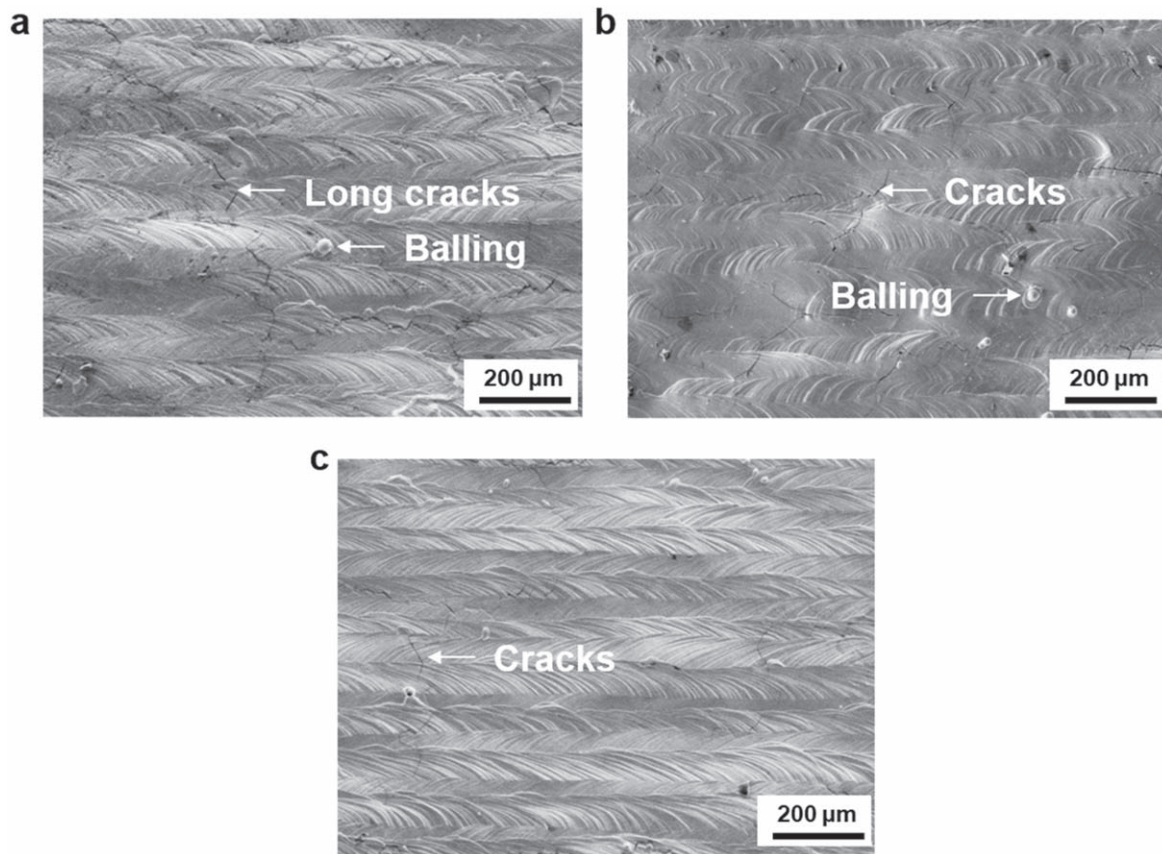


**Figure 3.** SEM images showing the surface morphologies of SLM-processed tungsten parts at different scanning strategies on the top view: (a) chessboard scanning strategy, (b) zigzag scanning strategy, (c) remelting scanning strategy.

load and dwell time were 0.3 kg and 15 s, respectively. For each sample, the microhardness of front view and side view was measured. A CMT5205 testing machine (MTS Industrial Systems, China) was used for compressive tests at the room temperature.

### 3. Results and discussion

#### 3.1. Surface morphology after solidification

Due to the nature of metallurgical bonding between layer and layer of SLM, the forming quality of each layer has an important impact on the subsequent forming process. Moreover, the laser scanning strategy directly influences the forming quality of single layer. Therefore, obtaining a single layer of high quality is very vital. Figure 3 shows the SEM images of surface morphologies of SLM-processed tungsten on the top view using different scanning strategies. It was obvious that long cracks run across the scanning tracks when the chessboard scanning strategy was applied. The surface was uneven with fragments and the balling phenomenon was significant, as shown in figure 3(a). As the zigzag scanning strategy was used, the surface was flat with reduced cracks and the fragments were eliminated (figure 3(b)). However, the balling phenomenon was remained. When the remelting scanning strategy was employed, the surface was even with

clear scanning tracks and reduced cracks, the balling phenomenon was weakened vastly (figure 3(c)).

In order to reveal the effects of scanning strategies on the surface morphology in details, the surfaces of top view and front view of SLM-processed tungsten were polished. Figure 4 depicts the polished surface of top view and front view. As shown in figure 4(a), when a chessboard scanning strategy was used, residual pores and mass cracks with a reticulate shape were observed on the surface of the top view. While on the surface of the front view, long cracks parallel to the building direction and large residual pores were viewed. Moreover, it could be observed that the cracks went through the pores (figure 4(d)). As the scanning strategy changed to zigzag scanning strategy, both the surfaces of top view and front view presented a great difference, as depicted in figures 4(b) and (e). It was obvious that the cracks were reduced with discontinuity and the pores were decreased from the top view (figure 4(b)). From the front view, it could be seen that the long cracks changed to the short cracks along the building direction and the residual pores was reduced (figure 4(e)). While the scanning strategy was the remelting scanning strategy, the surface of the top view was free of pores and only the tiny cracks could be seen (figure 4(c)). Similarly, the cracks on the surface of the front view were reduced and the pores were eliminated (figure 4(f)).

It is known to all that defects formation are a critical issue in the SLM process [41]. The common defects are pores,

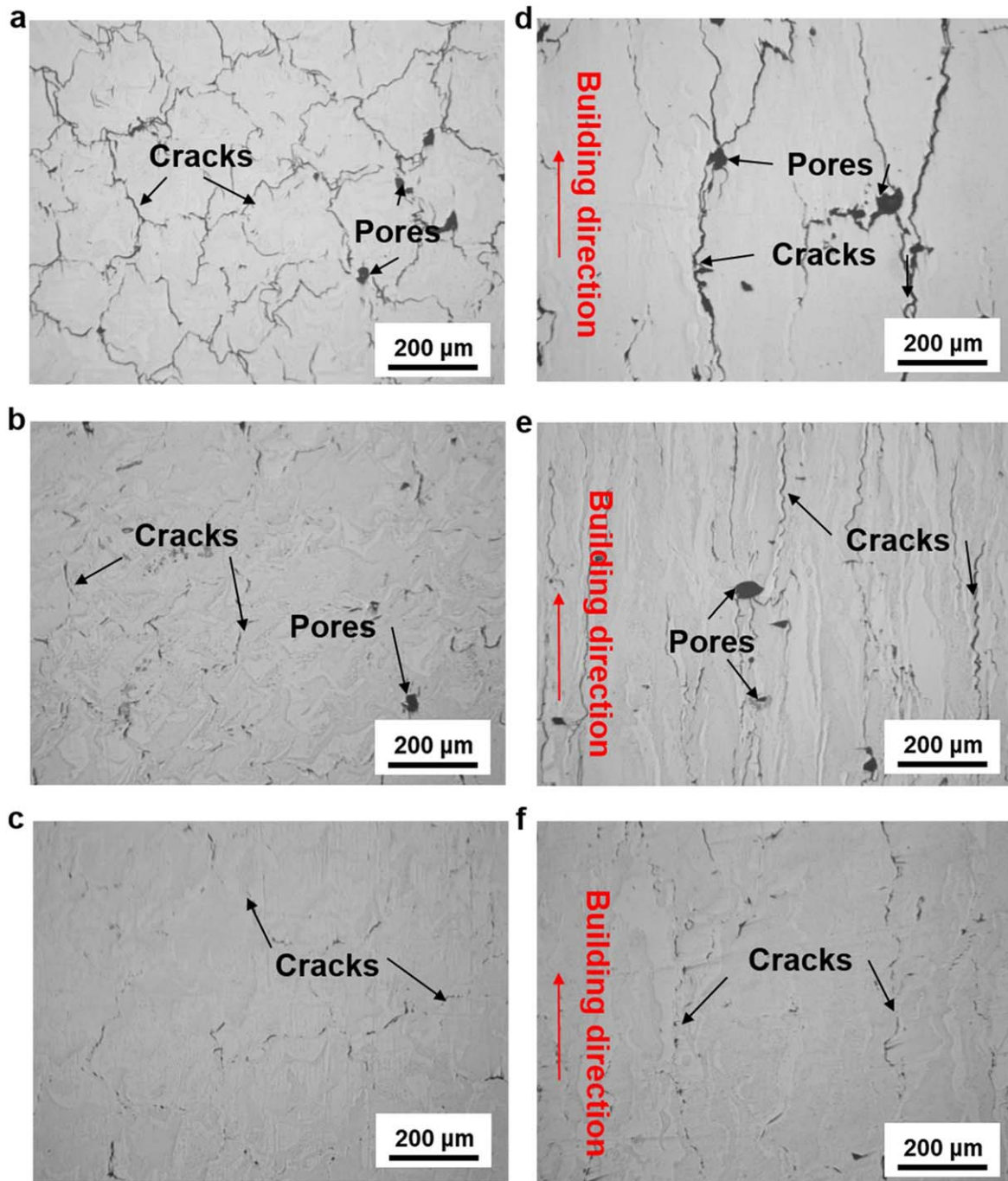


**Figure 4.** OM images showing the polished surface morphologies of SLM-processed tungsten parts at different scanning strategies on the top view and the front view: (a), (d) chessboard scanning strategy, (b), (e) zigzag scanning strategy, (c), (f) remelting scanning strategy.

cracks, impurities and distortion, etc. These defects are detrimental to the mechanical properties of final fabricated parts. For SLM-processed tungsten parts, cracks and pores are the primary defects. Several reasons can account for the formation of pores. Firstly, due to the high melting point of tungsten ( $\sim 3420^\circ\text{C}$ ), the laser energy density may be insufficient to melt the powder particles completely. Moreover, the laser absorptivity of tungsten is limited, indicating that the powder particles are unable to absorb the total energy. Therefore, the unmelted particles can cause the formation of pores. Secondly, tungsten has the high surface tension and viscosity

compared to other metal materials, which can cause worse balling phenomenon [42–44]. As demonstrated by Zhou *et al*, the solidification time of tungsten is only half of the spreading time regardless of the ambient temperature [37]. In this case, the balling tendency of tungsten can be large and resultant pores. Thirdly, high energy input can cause intense Marangoni flow in the molten pool, aggravating elements evaporation and resultant gas pores. It is widely believed that cracks are prone to generate due to the nature of fast solidification and rapid cooling [52]. However, high DBTT is an inherent characteristic for tungsten. During the SLM process,

the materials inevitably encounter the brittle temperature range when solidifying. Meanwhile, the shrinkage will happen during the solidification process. Under the joint effects of brittleness and shrinkage, cracks in SLM-processed tungsten are unavoidable. Compared three types of scanning strategies, it can be found that pores and cracks are prone to form when using the chessboard and zigzag scanning strategy. Generally, the single layer is divided into several small islands when applied a chessboard scanning strategy, the laser beam randomly selects small islands and melts the powder particles in the region. Due to the randomness of selection, the chessboard scanning strategy can lead to the discontinuous energy transfer during SLM process, causing the non-uniform energy distribution between island and island. Due to the non-uniform energy distribution, the temperature at the edge of the island is far below the internal region. During the cooling process, the shrinkage of the inside region is more serious than the edge. Therefore, the cracks are easy to generate in the inside region and finally form a reticular shape, as shown in figure 4(a). Meanwhile, the non-uniform shrinkage can accumulate between layer and layer, resulting in the long cracks parallel to the building direction (figure 4(d)). For the zigzag scanning strategy, the continuous laser-scanning mode can bring continuous heat transfer. Although the shrinkage during solidification is evitable, the cracks on the surfaces of the top view (figure 4(b)) and the front view (figure 4(e)) can be reduced due to the continuous scanning mode. As the laser remelting scanning strategy is applied, the defects are suppressed significantly. For the laser remelting scanning strategy, the single layer is melted two times. In this process, the previous unmelted powder particles can be melted completely and the pores can be eliminated, which is beneficial to the SLM process. Moreover, the laser remelting is equivalent to preheat the as-built layer, which can reduce the residual stress. Therefore, the cracks on the top view (figure 4(c)) and front view (figure 4(f)) are decreased.

### 3.2. Microstructure and mechanical properties

The scanning strategy plays a great role in determining the growth morphology of crystals. The morphology of crystals has an important effect on mechanical properties in turn. Figure 5 depicts the microstructures of three scanning strategies from the top view and the front view. It was obvious that the grain boundaries and defects could be distinguished clearly after etched. As shown in figure 5(a), the microstructure of SLM-processed tungsten was equiaxial columnar grains and divided into several regions by the cracks from the top view when using a chessboard scanning strategy. Besides, the residual pores and cracks were observed on the top view. From the front view, it was apparent that the columnar grains were parallel to the building direction (figure 5(d)). Moreover, the long cracks along the grain boundaries could be clearly distinguished. As the zigzag scanning strategy was used, the grains of the top view grew along the scanning direction with an equiaxial shape, presenting a consistent orientation (figure 5(b)). While the microstructures of the front view were columnar grains with a slender shape (figure 5(e)). The cracks

were reduced on both the top view and the front view. When the laser remelting scanning strategy was applied, it could be seen that both the microstructures of the top view and the front view were coarsened, as shown in figures 5(c) and (f). However, the cracks were reduced vastly. According to the classical solidification theory, the formation of columnar grain is mainly influenced by the direction of decreasing temperature [53]. During the SLM process, the direction of cooling tends to be perpendicular to the molten pool boundary, as shown in figure 6(a). The columnar grains grow along the direction of cooling in the molten pool. As the SLM process continues, the cooling direction gradually changes and is perpendicular to the as-built layer, as can be seen in figure 6(b). Due to the layer-wise feature of SLM, the microstructures gradually grow into coarse columnar regions with strong anisotropy (figure 6(c)), which is detrimental to the mechanical properties of SLM-processed tungsten parts.

Figure 7 shows the microhardness of SLM-processed tungsten parts under different scanning strategies. Both the microhardness of the top view and the front view was measured, respectively. The microhardness measured from the top view under different scanning strategies was shown in figure 7(a). The maximum microhardness of 490 HV was obtained when the zigzag scanning strategy was used. The microhardness of the chessboard scanning strategy and remelting scanning strategy was 474 HV and 439 HV, respectively. From the front view (figure 7(b)), it was clearly viewed that the maximum microhardness of 447 HV was obtained under the zigzag scanning strategy. While the minimum microhardness was 426 HV when the remelting scanning strategy was applied. The obtained microhardness of the chessboard scanning strategy was 432 HV. Compared the microhardness under three different scanning strategies, it could be concluded that the microhardness under the remelting scanning strategy was the lowest. However, the microhardness under the chessboard and zigzag scanning strategy had little difference. The reason for the low microhardness was the coarse microstructure caused by serious heat accumulation. Although the defects such as pores and cracks were reduced using a remelting scanning strategy, the microstructure was coarse, which was detrimental to the mechanical properties. Moreover, the microhardness of the top view and the front view was different regardless of the applied scanning strategies, which was owing to the anisotropy of columnar grains.

Figure 8 is the compressive stress-strain curves of SLM-processed tungsten parts at different scanning strategies. The direction of compressive load was parallel to the building direction. It was apparent that a compressive strength of 923 MPa and an elongation of 7.7% were obtained when the zigzag scanning strategy was applied, which was the highest among the three scanning strategies. However, the compressive strength and elongation of the remelting scanning strategy showed the lowest values of 755 MPa and 6%, respectively. While the obtained compressive strength and elongation were 902 MPa and 6.4% under the chessboard scanning strategy. Furthermore, table 1 shows the mechanical performances of pure W processed by different manufacturing



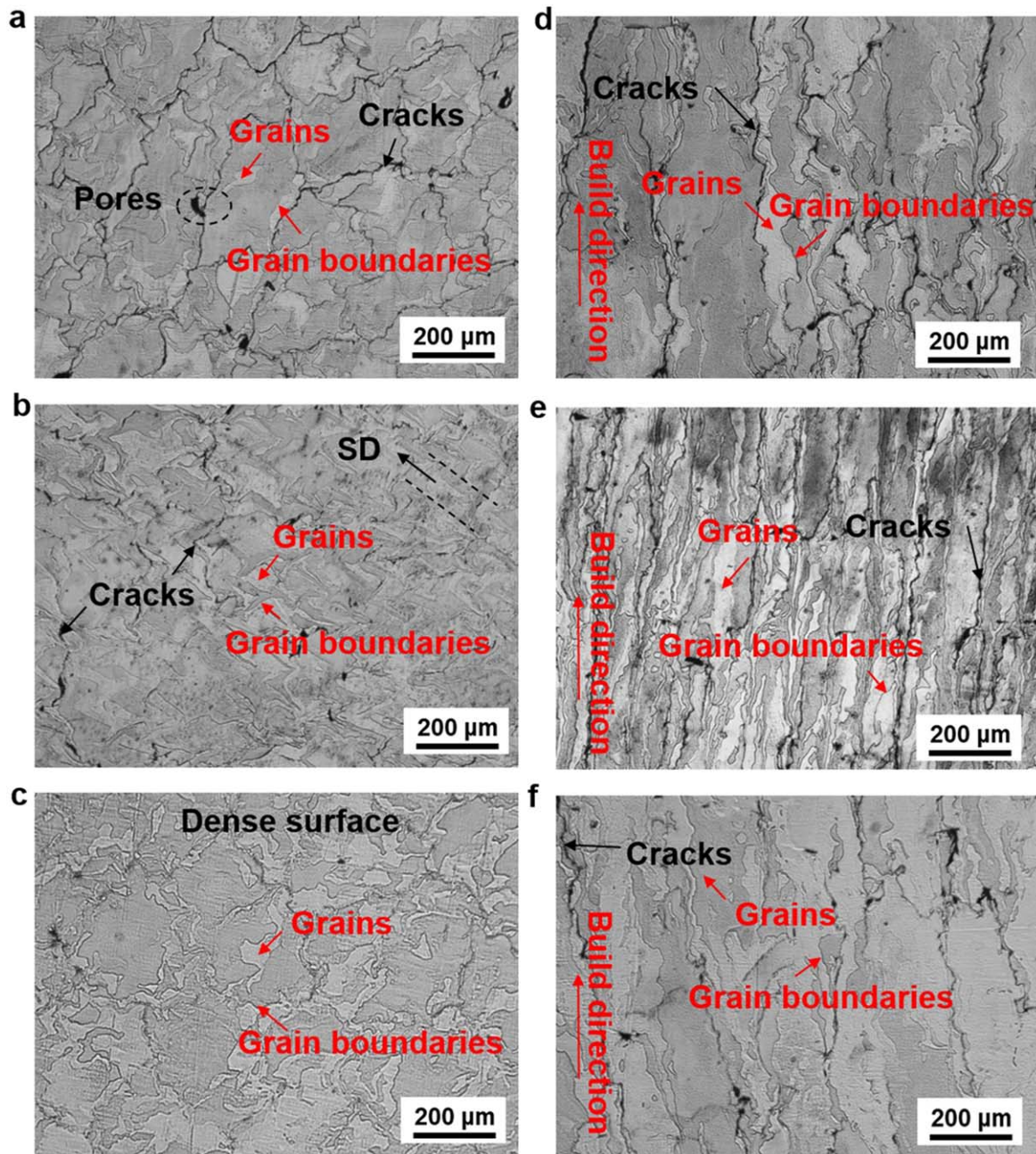


**Figure 5.** OM images showing the microstructures of SLM-processed tungsten parts at different scanning strategies on the top view and the front view: (a), (d) chessboard scanning strategy, (b), (e) zigzag scanning strategy, (c), (f) remelting scanning strategy. SD represents the scanning direction.

methods. It was obvious that the SLM-processed tungsten parts using zigzag scanning strategy demonstrated an excellent performance both in compressive strength and micro-hardness, indicating that SLM was an available method to fabricate tungsten.

In order to reveal the fracture mechanisms under different scanning strategies, the fracture morphologies were depicted in figure 9. When the chessboard scanning strategy was applied, the fracture surface was uneven with apparent pores and cracks, as shown in figure 9(a). The cleavage steps could be seen clearly at high magnifications (figure 9(d)), which was the typical feature of brittle fracture. As the scanning

strategy changed to zigzag scanning strategy, the fracture morphology showed a certain direction along the scanning direction, as shown in figure 9(b). Moreover, the reduced pores and cracks were observed on the uneven fracture. At high magnifications, the cleavage steps were obvious (figure 9(e)). When the strategy was remelting scanning strategy, the flat fracture was observed with cracks (figure 9(c)). High magnifications of fracture morphology showed that the fracture was smooth with clear cleavage facets (figure 9(f)).

Based on the observations of fracture morphologies, it could be concluded that the fracture of SLM-processed



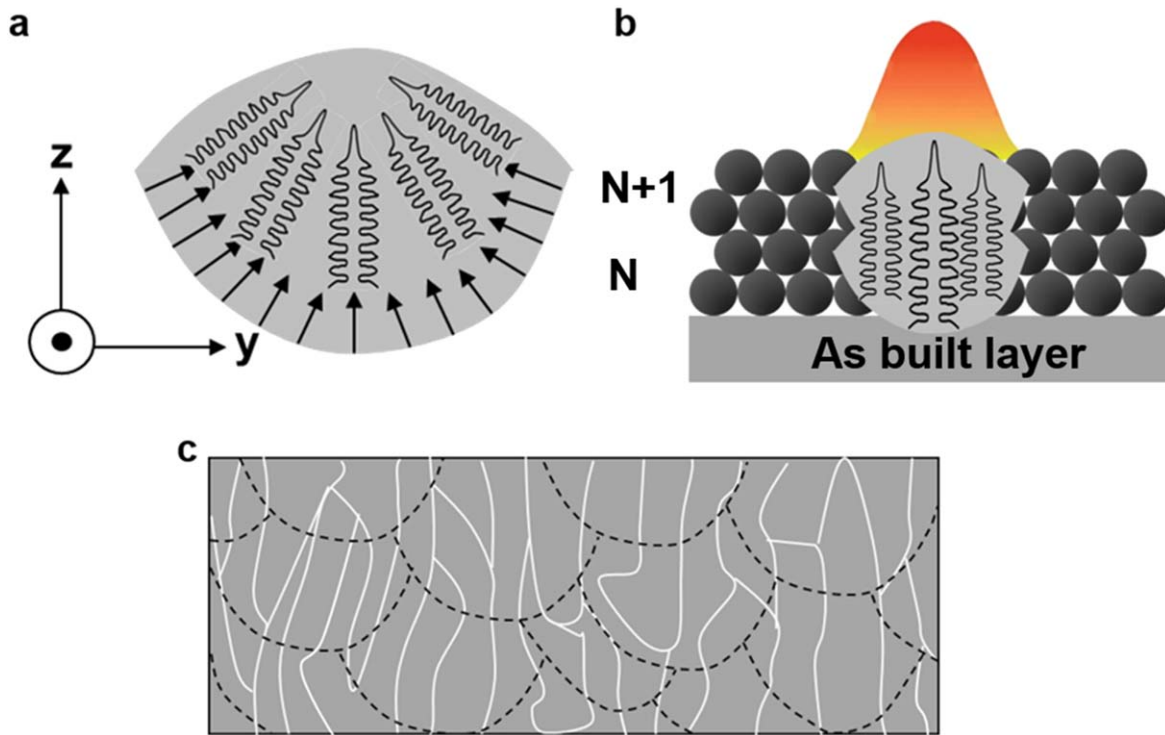


**Figure 6.** Schematic illustrations of the formation mechanism of columnar crystals of SLM-processed pure tungsten, (a) the growth orientation of columnar crystals in a single molten pool, (b) the growth pattern of columnar crystals between layers, (c) the grain structures of SLM-processed pure tungsten on the front view.

tungsten parts demonstrated typical characteristic of brittle fracture with few plastic deformations [49]. It is generally acknowledged that the mechanical properties of materials are determined by the microstructures. The defects of pores and cracks were account for the early failure when the chessboard and zigzag scanning strategies were used. For the chessboard scanning strategy, when the compressive load was applied, the breakage was driven from the reticular cracks and gradually propagated along the long cracks on the front view. Finally, the uneven fracture morphology divided by the reticular cracks was formed, as shown in figure 9(a). As the zigzag scanning strategy was employed, the sequential laser-scanning path can induce the formation of microstructures having the same growth orientation. The microstructures owning this characteristic would fracture along the scanning direction when forced by a compressive load. As a result, the uneven fracture with a certain direction was formed, which was depicted in figure 9(b). When the remelting scanning strategy was applied, the obtained microstructures were coarse. According to the Hall–Petch equation [50]:

$$\sigma_y = \sigma_0 + k_y d^{-\frac{1}{2}}, \quad (1)$$

where  $\sigma_y$  represents the yield stress of materials,  $\sigma_0$  is the friction resistance of a lattice when moving a single dislocation,  $k_y$  is a constant related to the type of material and grain size, and  $d$  represents the average grain diameter. This formula demonstrated that the strength of materials has a negative correlation with the grain size. Although the defects of SLM-processed tungsten parts at the remelting scanning

strategy were the least among three scanning strategies. The grain size of microstructures under the remelting scanning strategy was the largest. As a result, the compressive strength was the lowest. Moreover, due to the decreased number of grain boundaries resulted by the grain coarsening, the fracture was flat and the feature of cleavage steps were not obvious, as shown in figures 9(c) and (f).

### 3.3. EBSD analysis of SLM-processed tungsten parts

It is known to all that the properties of the material are determined by its microstructures. Therefore, to further reveal the reasons of variation in compressive strength caused by the microstructural difference. The microstructures of SLM-processed tungsten parts were detected by EBSD. For better comparison, the zigzag scanning strategy with the highest compressive strength and the remelting scanning strategy having the lowest compressive strength were studied. Figure 10 presents the EBSD orientation maps of the zigzag scanning strategy and the remelting scanning strategy along the build direction. The detection regions were selected from the front view of the as-fabricated samples. For the zigzag scanning strategy, the columnar grain bands composed of many slender columnar crystals could be clearly distinguished, as shown in figure 10(a). The grain size of the columnar grains was about 30  $\mu\text{m}$ . Moreover, the columnar grain bands were parallel to the building direction, which indicated that the columnar grains presented a strong epitaxial growth along the building direction. However, as the remelting scanning strategy was applied, the growth direction

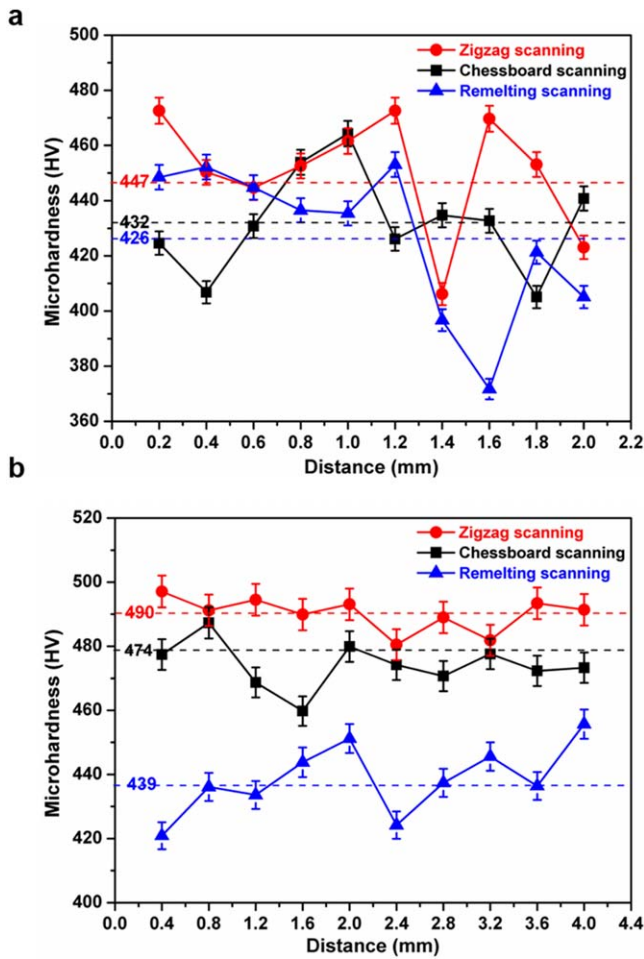


**Figure 7.** The microhardness of SLM-processed tungsten parts at different scanning strategies on the top view (a) and the front view (b).

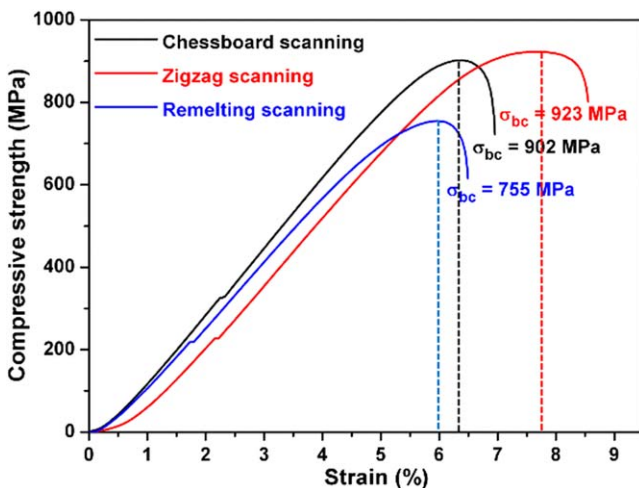


**Figure 8.** Compressive stress–strain curves for SLM-processed pure tungsten samples at different scanning strategies.

of columnar grains was deviated from the building direction, as shown in figure 10(b). Besides, the grains grew obviously with a grain size of  $45 \mu\text{m}$ . Figure 11 depicts the pole figure (PF) and inverse pole figure maps of SLM-processed tungsten

**Table 1.** Comparison of mechanical performance of pure W by different processing methods.

Processing methods	Compressive strength (MPa)	Microhardness (HV)
SLM	923	490
PM [11, 45]	1000–1200	445
SPS [46, 47]	980	302
CVD [48]	780	419

parts at the zigzag scanning strategy and the remelting scanning strategy. The results were measured from the front view along the building direction. The PF maps quantified that the texture intensities for the three crystallographic direction families were  $\langle 001 \rangle$ ,  $\langle 101 \rangle$  and  $\langle 111 \rangle$ . For the zigzag scanning strategy, a strong  $\langle 001 \rangle$  texture along the transverse direction (TD) was observed (figure 11(a)). However, as the scanning strategy changed to the remelting scanning strategy, a strong texture of  $\langle 111 \rangle$  was viewed along the TD, as shown in figure 11(b). The microstructure of SLM-processed tungsten by the remelting scanning strategy showed a stronger anisotropy with a maximum intensity of 11.54. It could be found that there was nearly no strong texture along the BD. It is known to all that the crystallographic texture has a significant effect on the mechanical properties of materials. The existence of texture makes the properties of materials show anisotropy. For bcc metals, it is generally reported that a preferred  $\langle 100 \rangle$  growth direction during solidification and a  $\langle 001 \rangle$  fiber texture parallel to the building direction are prone to form when produced by powder bed AM [51, 54]. However, the SLM-processed tungsten parts in this work presented a different texture due to the various applied scanning strategies. Moreover, the growth direction of the columnar grains was changed when the applied scanning strategy was changed from the zigzag scanning strategy to the remelting scanning strategy. Due to the deviation of growth direction of columnar grains caused by the remelting scanning strategy, a shear stress would be generated when the compressive load was applied, resulting in the decrease in compressive strength.

#### 4. Conclusions

In this work, three types of scanning strategies including the chessboard scanning strategy, the zigzag scanning strategy and the remelting scanning strategy were adopted to produce the pure tungsten samples by SLM. The effects of scanning strategies on the surface morphology of solidification, microstructure, mechanical properties and crystallographic texture were investigated in detail. The main conclusions are as follows.

- (1) The scanning strategies had a great influence on the surface morphology of SLM-processed tungsten parts. The defects such as pores and cracks were prone to generate when applying the chessboard scanning strategy or the zigzag scanning strategy. The remelting

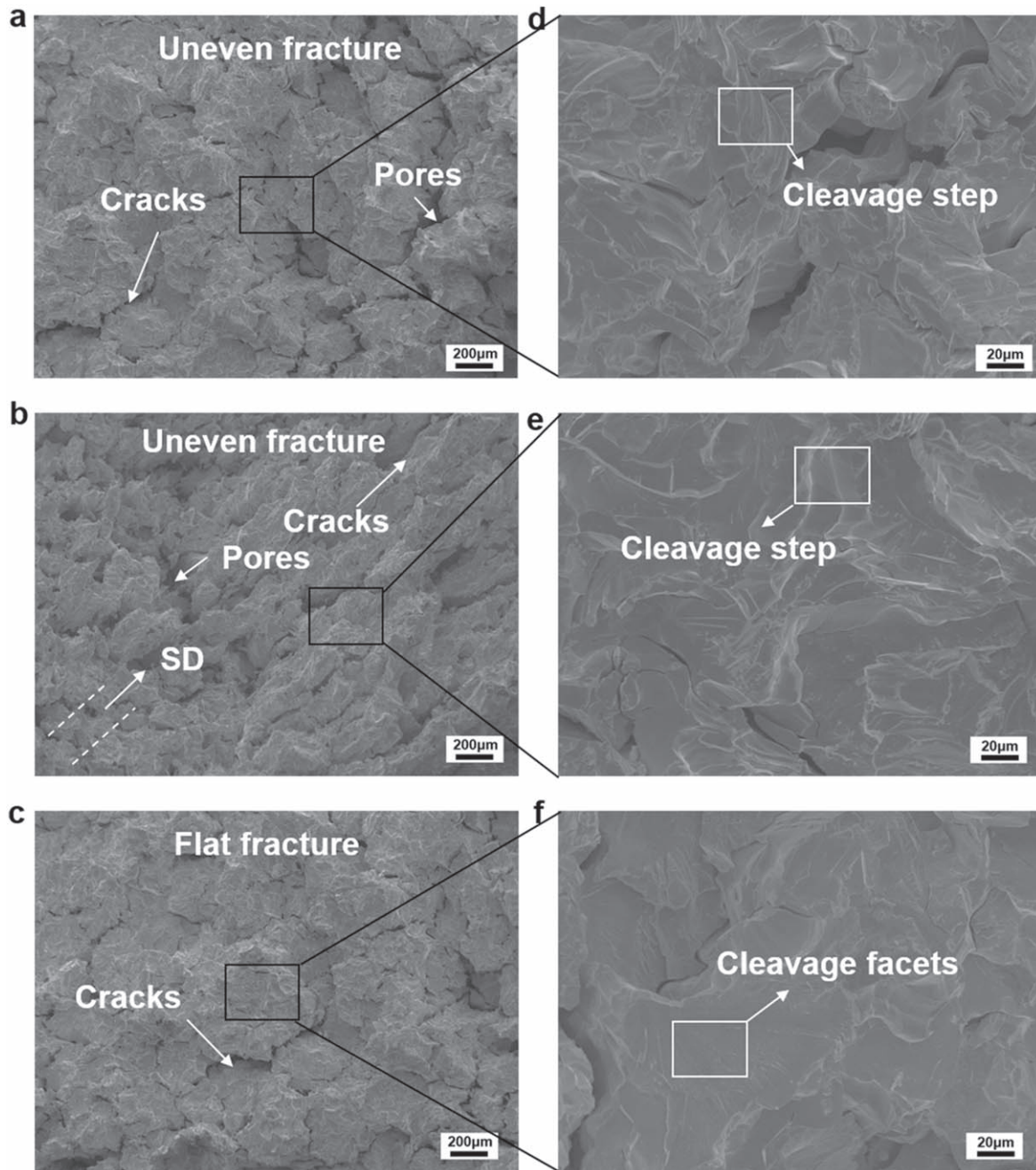


**Figure 9.** SEM images showing the fracture morphologies of SLM-processed tungsten parts at different scanning strategies: (a), (d) chessboard scanning strategy, (b), (e) zigzag scanning strategy, (c), (f) remelting scanning strategy.

scanning strategy could eliminate the pores and reduce the cracks, which was recommended to produce components with good surface quality and less defects.

- (2) The microstructure of SLM-processed tungsten parts was columnar grain regardless of the applied scanning strategies. The formation of the columnar grains was due to the heat transfer direction during SLM process. The columnar grains of SLM-processed tungsten parts showed anisotropy in microhardness.
- (3) The scanning strategies had a significant impact on the compressive strength of SLM-processed tungsten parts. Although the cracks were inevitable, the compressive strength obtained under the chessboard scanning

strategy and the zigzag scanning strategy was higher than the remelting scanning strategy. For the acquisition of good performance, the zigzag scanning strategy was preferential.

- (4) The microstructure determined the properties of materials in a large part. The microstructure under the zigzag scanning strategy had more grain boundaries than the remelting scanning strategy, which was an important reason accounting for the high compressive strength. As the scanning strategy changed from the zigzag scanning strategy to the remelting scanning strategy, the crystallographic orientation changed from  $\langle 001 \rangle$  to  $\langle 111 \rangle$  along the TD.



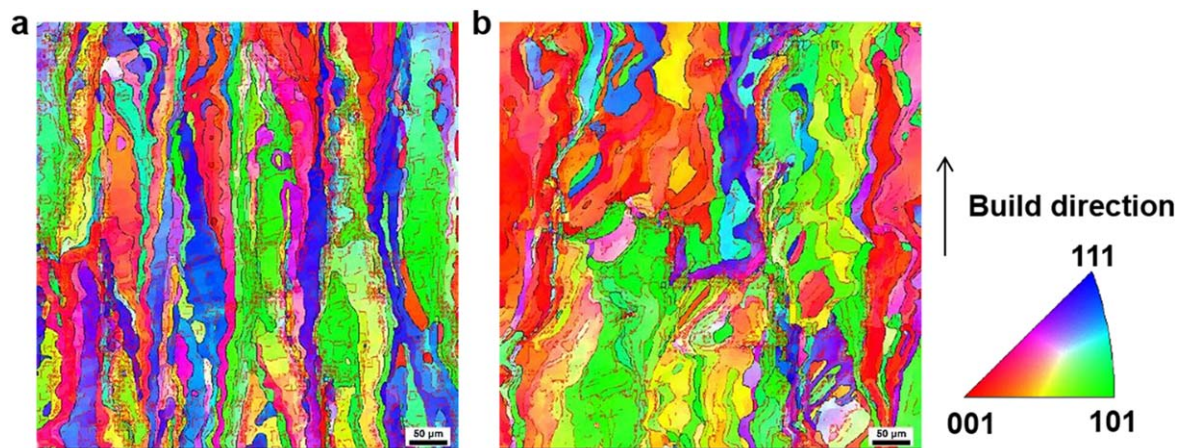


**Figure 10.** EBSD orientation maps from the front view of (a) zigzag scanning strategy, (b) remelting scanning strategy.

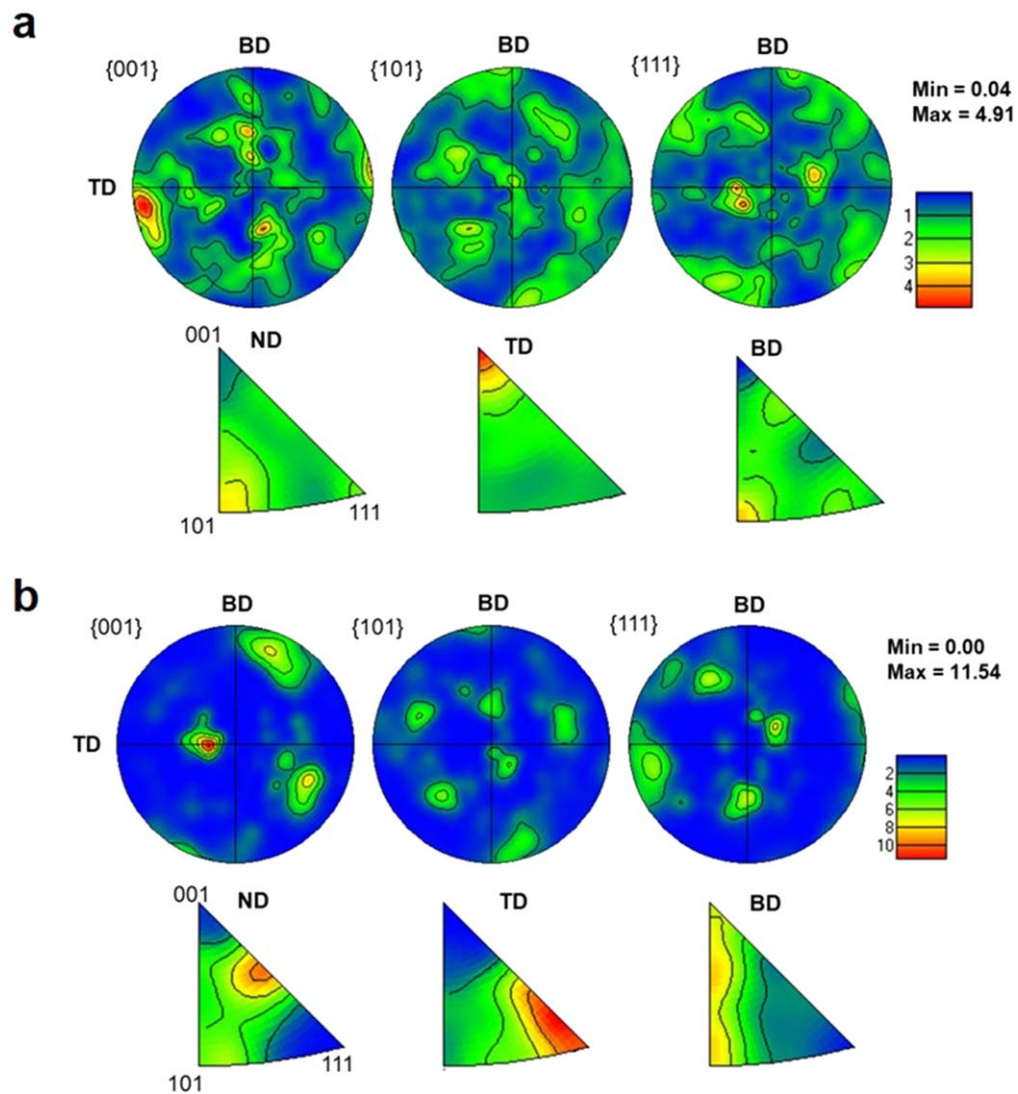


**Figure 11.** Pole figure (PF) and inverse pole figure (IPF) maps measured from the front view of as-fabricated samples at (a) zigzag scanning strategy and (b) remelting scanning strategy. ND, TD and BD represent normal direction ( $x$ ), transverse direction ( $y$ ) and building direction ( $z$ ), respectively.

## Acknowledgments

The authors gratefully acknowledge the financial support by Science Challenge Project (Nos. TZ2018006-0301-02 and TZ2018006-0303-03); National Natural Science Foundation of China (No. 51735005); National Natural Science Foundation of China for Creative Research Groups (Grant No. 51921003). Meng Guo thanks the Priority Academic Program Development of Jiangsu Higher Education Institutions.

## ORCID iDs

Dongdong Gu  <https://orcid.org/0000-0002-8258-6935>

## References

- [1] Knapp V and Pevec D 2018 Promises and limitations of nuclear fission energy in combating climate change *Energy Policy* **120** 94–9
- [2] Entler S, Horacek J, Dlouhy T and Dostal V 2018 Approximation of the economy of fusion energy *Energy* **152** 489–97
- [3] Rowcliffe A F, Garrison L M, Yamamoto Y, Tan L and Katoh Y 2018 Materials challenges for the fusion nuclear science facility *Fusion Eng. Des.* **135** 290–301
- [4] Schmid K, Rieger V and Manhard A 2012 Comparison of hydrogen retention in W and W/Ta alloys *J. Nucl. Mater.* **426** 247–53
- [5] Rieth M et al 2013 Recent progress in research on tungsten materials for nuclear fusion applications in Europe *J. Nucl. Mater.* **432** 482–500
- [6] Neu R et al 2016 Advanced tungsten materials for plasma-facing components of DEMO and fusion power plants *Fusion Eng. Des.* **109–111** 1046–52
- [7] Prakash C, Lee H, Alucozai M and Tomar V 2016 An analysis of the influence of grain boundary strength on microstructure dependent fracture in polycrystalline tungsten *Int. J. Fract.* **199**
- [8] Ren C, Fang Z Z, Koopman M, Butler B, Paramore J and Middlemas S 2018 Methods for improving ductility of tungsten—a review *Int. J. Refract. Met. Hard Mater.* **75** 170–83
- [9] Wang J, Zhao G, Chen L and Li J 2016 A comparative study of several constitutive models for powder metallurgy tungsten at elevated temperature *Mater. Des.* **90** 91–100
- [10] Antusch S, Hoffmann J, Klein A, Gunn J P, Rieth M and Weingaertner T 2018 Processing of complex near-net-shaped tungsten parts by PIM *Nucl. Mater. Energy* **16** 71–5
- [11] Senthilnathan N, Annamalai A R and Venkatachalam G 2018 Synthesis of tungsten through spark plasma and conventional sintering processes *Mater. Today Proc.* **5** 7954–9
- [12] Zolfaghari A, Chen T and Yi A Y 2019 Additive manufacturing of precision optics at micro and nanoscale *Int. J. Extrem. Manuf.* **1** 012005
- [13] Gu D D, Meiners W, Wissenbach K and Poprawe R 2012 Laser additive manufacturing of metallic components: materials, processes and mechanisms *Int. Mater. Rev.* **57** 133–64
- [14] Yap C Y, Chua C K, Dong Z L, Liu Z H, Zhang D Q, Loh L E and Sing S L 2015 Review of selective laser melting: materials and applications *Appl. Phys. Rev.* **2** 041101
- [15] Olakanmi E O, Cochrane R F and Dalgarno K W 2015 A review on selective laser sintering/melting (SLS/SLM) of aluminium alloy powders: processing, microstructure, and properties *Prog. Mater. Sci.* **74** 401–77
- [16] Herzog D, Seyda V, Wycisk E and Emmelmann C 2016 Additive manufacturing of metals *Acta Mater.* **117** 371–92
- [17] Zhang S, Cheng X, Yao Y, Wei Y, Han C, Shi Y, Wei Q and Zhang Z 2015 Porous niobium coatings fabricated with selective laser melting on titanium substrates: Preparation, characterization, and cell behavior *Mater. Sci. Eng. C* **53** 50–9
- [18] Gu D, Shi Q, Lin K and Xi L 2018 Microstructure and performance evolution and underlying thermal mechanisms of Ni-based parts fabricated by selective laser melting *Addit. Manuf.* **22** 265–78
- [19] Gu D, Zhang H, Dai D, Xia M, Hong C and Poprawe R 2019 Laser additive manufacturing of nano-TiC reinforced Ni-based nanocomposites with tailored microstructure and performance *Composites B* **163** 585–97
- [20] Ma C, Gu D, Dai D, Zhang H, Zhang H, Yang J, Guo M, Du Y and Gao J 2019 Microstructure evolution and high-temperature oxidation behaviour of selective laser melted TiC/TiAl composites *Surf. Coat. Technol.* **375** 534–43
- [21] Gu D, Rao X, Dai D, Ma C, Xi L and Lin K 2019 Laser additive manufacturing of carbon nanotubes (CNTs) reinforced aluminum matrix nanocomposites: processing optimization, microstructure evolution and mechanical properties *Addit. Manuf.* **29** 100801
- [22] Wang D Z, Li K L, Yu C F, Ma J, Liu W and Shen Z J 2019 Cracking behavior in additively manufactured pure tungsten *Acta Metall. Sin.* **32** 127–35
- [23] Faidel D, Jonas D, Natour G and Behr W 2015 Investigation of the selective laser melting process with molybdenum powder *Addit. Manuf.* **8** 88–94
- [24] Zhou L, Yuan T, Li R, Tang J, Wang G and Guo K 2017 Selective laser melting of pure tantalum: densification, microstructure and mechanical behaviors *Mater. Sci. Eng. A* **707** 443–51
- [25] Wang D, Yu C, Ma J, Liu W and Shen Z 2017 Densification and crack suppression in selective laser melting of pure molybdenum *Mater. Des.* **129** 44–52
- [26] Wen S, Wang C, Zhou Y, Duan L, Wei Q, Yang S and Shi Y 2019 High-density tungsten fabricated by selective laser melting: densification, microstructure, mechanical and thermal performance *Opt. Laser Technol.* **116** 128–38
- [27] Iveković A, Omidvari N, Vrancken B, Lietaert K, Thijs L, Vanmeensel K, Vleugels J and Kruth J P 2018 Selective laser melting of tungsten and tungsten alloys *Int. J. Refract. Met. Hard Mater.* **72** 27–32
- [28] Wang D, Yu C, Zhou X, Ma J, Liu W and Shen Z 2017 Dense pure tungsten fabricated by selective laser melting *Appl. Sci.* **7** 430
- [29] Enneti R K, Morgan R and Atre S V 2018 Effect of process parameters on the Selective Laser Melting (SLM) of tungsten *Int. J. Refract. Met. Hard Mater.* **71** 315–9
- [30] Yu W, Sing S L, Chua C K and Tian X 2019 Influence of re-melting on surface roughness and porosity of AlSi10Mg parts fabricated by selective laser melting *J. Alloys Compd.* **574**–81
- [31] Wan H Y, Zhou Z J, Li C P, Chen G F and Zhang G P 2018 Effect of scanning strategy on grain structure and crystallographic texture of Inconel 718 processed by selective laser melting *J. Mater. Sci. Technol.* **34** 1799–804
- [32] Yasa E and Kruth J P 2011 Microstructural investigation of selective laser melting 316L stainless steel parts exposed to laser re-melting *Proc. Eng.* **19** 389–95
- [33] Sun S H, Hagihara K and Nakano T 2018 Effect of scanning strategy on texture formation in Ni-25 at%Mo alloys fabricated by selective laser melting *Mater. Des.* **140** 307–16

- [34] Geiger F, Kunze K and Etter T 2016 Tailoring the texture of IN738LC processed by selective laser melting (SLM) by specific scanning strategies *Mater. Sci. Eng. A* **661** 240–6
- [35] Yasa E, Kruth J P and Deckers J 2011 Manufacturing by combining selective laser melting and selective laser erosion/laser re-melting *CIRP Ann.—Manuf. Technol.* **60** 263–6
- [36] Dai D, Gu D, Zhang H, Xiong J, Ma C, Hong C and Poprawe R 2018 Influence of scan strategy and molten pool configuration on microstructures and tensile properties of selective laser melting additive manufactured aluminum based parts *Opt. Laser Technol.* **99** 91–100
- [37] Zhou X, Liu X, Zhang D, Shen Z and Liu W 2015 Balling phenomena in selective laser melted tungsten *J. Mater. Process. Technol.* **222** 33–42
- [38] Wang D, Wang Z, Li K, Ma J, Liu W and Shen Z 2019 Cracking in laser additively manufactured W: initiation mechanism and a suppression approach by alloying *Mater. Des.* **162** 384–93
- [39] Braun J, Kaserer L, Stajkovic J, Leitz K H, Tabernig B, Singer P, Leibenguth P, Gspan C, Kestler H and Leichtfried G 2019 Molybdenum and tungsten manufactured by selective laser melting: analysis of defect structure and solidification mechanisms *Int. J. Refract. Met. Hard Mater.* **84** 104999
- [40] Guo M, Gu D, Xi L, Zhang H, Zhang J, Yang J and Wang R 2019 Selective laser melting additive manufacturing of pure tungsten: role of volumetric energy density on densification, microstructure and mechanical properties *Int. J. Refract. Met. Hard Mater.* **84** 105025
- [41] Zhang B, Li Y and Bai Q 2017 Defect formation mechanisms in selective laser melting: a review *Chin. J. Mech. Eng.* **30** 515–27
- [42] Mills K C, Su Y, Li Z and Brooks R F 2004 Equations for the calculation of the thermo-physical properties of stainless steel *ISIJ Int.* **44** 1661–8
- [43] Keene B J 2014 Review of data for the surface tension of pure metals *Int. Mater. Rev.* **38** 157–92
- [44] Paradis P F, Ishikawa T and Yoda S 2005 Viscosity of liquid undercooled tungsten *J. Appl. Phys.* **97** 106101
- [45] Huang H, Wu Y Q, Wang S L, He Y H, Zou J, Huang B Y and Liu C T 2009 Mechanical properties of single crystal tungsten microwhiskers characterized by nanoindentation *Mater. Sci. Eng. A* **523** 193–8
- [46] Lee J, Kim S, Ott R T, Kim J, Eckert J and Lee M 2015 Effect of reinforcement phase on the mechanical property of tungsten nanocomposite synthesized by spark plasma sintering *Int. J. Refract. Met. Hard Mater.* **54** 14–8
- [47] Ma J, Zhang J, Liu W and Shen Z 2013 Suppressing pore-boundary separation during spark plasma sintering of tungsten *J. Nucl. Mater.* **438** 199–203
- [48] Yanwei L, Xiaodong Y, Chengwen T, Tiefeng S, Kunsong M and Hongnian C 2011 Effect of the  $\beta$  phase on compressive mechanical property of CVD tungsten *Rare Met. Mater. Eng.* **40** 1138–40
- [49] Ren C, Fang Z Z, Xu L, Ligda J P, Paramore J D and Butler B G 2019 An investigation of the microstructure and ductility of annealed cold-rolled tungsten *Acta Mater.* **162** 202–13
- [50] Hansen N 2004 Hall–Petch relation and boundary strengthening *Scr. Mater.* **51** 801–6
- [51] Livescu V, Knapp C M, Gray G T, Martinez R M, Morrow B M and Ndefu B G 2018 Additively manufactured tantalum microstructures *Materialia* **1** 15–24
- [52] Arunkumar S, Rangarajan P, Devakumaran K and Sathiya P 2015 Comparative study on transverse shrinkage, mechanical and metallurgical properties of AA2219 aluminium weld joints prepared by gas tungsten arc and gas metal arc welding processes *Def. Technol.* **11** 262–8
- [53] Tsuchiya S, Ohno M, Matsuura K and Isobe K 2011 Formation mechanism of coarse columnar  $\gamma$  grains in as-cast hyperperitectic carbon steels *Acta Mater.* **59** 3334–42
- [54] Sidambe A T, Tian Y, Prangnell P B and Fox P 2019 Effect of processing parameters on the densification, microstructure and crystallographic texture during the laser powder bed fusion of pure tungsten *Int. J. Refract. Met. Hard Mater.* **78** 254–63